Powder-to-Film Conversion of Nickel Single-Atom Catalysts into Binder-Free and Resistant Electrodes

M. Vigliengo, A. Frenkel

To be published in "Advanced Materials Interfaces"

February 2026

Chemistry Department
Brookhaven National Laboratory

U.S. Department of Energy
USDOE Office of Science (SC), Basic Energy Sciences (BES). Materials Sciences & Engineering Division (MSE)

DISCLAIMER

Advanced Materials Interfaces

ADVANCED MATERIALS INTERFACES
Open Access
www.advmatinterfaces.de

RESEARCH ARTICLE OPEN ACCESS

Powder-to-Film Conversion of Nickel Single-Atom Catalysts into Binder-Free and Resistant Electrodes

Milla Vigliengo[1] | Nicolò Allasia[1] | Shuting Xiang[2] | Yurii P. Ivanov[3] | Riccardo Gulminelli[1] | Martin Sterrer[4] | Giorgio Divitini[3] | Anatoly I. Frenkel[2,5] | Gianvito Vilé[1]

[1]Department of Chemistry, Materials and Chemical Engineering "Giulio Natta", Politecnico di Milano, Milano, Italy | [2]Materials Science and Chemical Engineering Department, Stony Brook University, Stony Brook, NY, USA | [3]Electron Spectroscopy and Nanoscopy Group, Istituto Italiano di Tecnologia (IIT), Genova, Italy | [4]Institute of Physics, University of Graz, Graz, Austria | [5]Chemistry Division, Brookhaven National Laboratory, Upton, NY, USA

Correspondence: Gianvito Vilé (gianvito.vile@polimi.it)

Received: 29 October 2025 | **Revised:** 7 December 2025 | **Accepted:** 7 December 2025

Keywords: carbon materials | earth-abundant metals | single-atom catalysis | spectroscopy | standalone electrodes

ABSTRACT

Although a few binder-free and self-supported single-atom electrodes have been reported, achieving mechanically robust, defect-engineered, and reproducible films that preserve atomic dispersion under electrochemical operation remains challenging. This work addresses this limitation by presenting a versatile and generalizable strategy to transform powders into standalone, defect-engineered thin films hosting atomically dispersed Ni centers within conductive 2D frameworks. The physicochemical and electronic properties of these materials are thoroughly characterized using a comprehensive set of spectroscopic and microscopic techniques and confirmed the homogeneous dispersion and monoatomic nature of the Ni centers (0.94 wt.%) on the electrode films. Electrochemical testing via cyclic voltammetry and electrochemical impedance spectroscopy under a range of experimental conditions revealed that integration of Ni single atoms markedly enhanced performance and stability compared to carbon nanotube-only electrodes, maintaining integrity after 15 h of continuous operation. This improvement is accompanied by a notable reduction in charge transfer resistance (30.50 Ω) and an increase in double-layer capacitance (295.45 µF). Post-electrochemical analyses corroborated the structural integrity and robustness of the electrodes. Overall, this work bridges atomically precise catalysis and device-level electrochemistry, opening a route toward reproducible and scalable single-atom electrodes for sensing and energy conversion.

1 | Introduction

The growing emphasis on sustainability in the chemical industry is driving the search for greener alternatives to conventional synthetic methodologies. Within this context, electrochemistry has emerged as a powerful platform for redox-driven chemical transformations [1, 2], eliminating the need for hazardous reducing or oxidizing agents and significantly reducing waste generation, in accordance with the principles of green chemistry [3]. In addition, electrochemical processes offer precise control over potential, current, and electrode surface properties, enabling enhanced selectivity and energy efficiency [4–9]. Recent advances in electrode design and reactor engineering have expanded the scope of electrochemical methods, enabling new applications for the production of pharmaceuticals, polymers, biosensors, and fine chemicals with reduced environmental impact [6–11].

Despite these advantages, reproducibility and scalability remain critical challenges in electrosynthesis, as subtle variations in electrode morphology, composition, or fabrication can strongly influence reaction performance [12, 13]. Although a variety of commercial electrodes are readily available, they are typically limited to metal-based (e.g., platinum wire, nickel foam, zinc or copper plates) and carbon-based materials (such as graphite and glassy carbon) [14, 15]. Moreover, these commercial materials often lack the structural precision or surface functionality required for specialized or advanced applications. Consequently, the design and synthesis of tailored, reproducible electrode materials have become central goals in modern electrochemical research. Among emerging materials, carbon-based nanostructures, including carbon nanotubes (CNTs) and graphene, have attracted substantial attention owing to their outstanding electrical conductivity, high surface area, and mechanical robustness [16]. Their physicochemical properties can be finely tuned through the incorporation of heteroatoms or isolated metal centers, which modulate charge distribution, local coordination, and electronic structure [17]. When such atomically dispersed metal sites are stabilized, they form single-atom catalysts (SACs) [18–27], which show remarkable performance in a wide range of transformations, including oxygen reduction reaction (ORR) [28–30], oxygen evolution reaction (OER) [31], hydrogen evolution reaction (HER) [32], and CO_2 reduction reaction (CO_2RR) [33]. Beyond energy conversion, their structural precision and controllable porosity also make them attractive for biosensing applications, enabling selective biorecognition and efficient detection of large biomolecules such as peptides and proteins [34–36].

Within this family, multi-walled carbon nanotubes (MWCNT) represent particularly versatile supports due to their large surface area, high conductivity, and exceptional mechanical strength [37–45]. Nevertheless, most SAC-based electrodes are still fabricated adding polymeric binders in the synthesis, in order to adhere catalyst powders onto conductive substrates [46, 47]. Although this approach simplifies processing, it introduces insulating domains, can block active sites, and compromise long-term stability. In contrast, binder-free architectures integrate the catalyst species directly into the carbon lattice, preventing site blockage and conductivity losses while ensuring full accessibility to active sites. As a result, such electrodes deliver superior performance and broader applicability compared to conventional binder-based designs. Examples of standalone films have also been reported [48, 49], but they remain comparatively rare because of the unresolved challenges in long-term mechanical and electrochemical stability under operating conditions. The absence of polymeric binders removes mechanical buffering and increases vulnerability to stress from gas bubble evolution, repeated wetting/dewetting cycles, and redox-induced lattice strain. These effects can lead to cracking in the electrode films, as well as pore collapse and partial delamination that may accelerate the degradation of such free-standing films [50]. Additionally, fabrication methodologies represent a major practical bottleneck. Although versatile strategies exist, many rely on costly equipment and energy-intensive processes, often requiring high operating temperatures (e.g., chemical vapor deposition (CVD), inkjet printing, sputtering). Conversely, more economically accessible routes, including hydro/solvothermal synthesis and vacuum filtration, typically require extended reaction times (up to 48 h) and provide limited control over film thickness and large-area uniformity. Despite significant advancements, the combination of insufficient mechanical durability, limited process control, and low-throughput manufacturing continue to hinder the scalable production of robust free-standing binder-free electrodes for implementation in practical electrosynthesis [51–53].

In this work, we present a versatile approach for designing and fabricating standalone, thin electrode films featuring Ni SACs supported on carbon nitride (CN_x) and MWCNT. Through comprehensive characterization of the material's morphology, composition, and electrochemical properties, we demonstrate the robustness and stability of the novel electrodes under a wide range of reaction conditions. Overall, the present introduces a reproducible powder-to-film conversion route that integrates atomic-level catalyst precision with device-scale robustness, enabling continuous operation over several hours, an advance beyond the short-term stability typical of existing binder-free electrodes.

2 | Materials and Methods

2.1 | Preparation of CN_x-Supported Ni SAC

A Ni SAC was synthesized following an established hard-template polymerization procedure reported in the literature [54, 55]. Initially, nickel(II) chloride ($NiCl_2$; 30 mg; Sigma–Aldrich, 98%) and cyanamide (1.2 g; Sigma–Aldrich, 99%) were dissolved in 3 mL of Milli-Q water, serving as the Ni source and N-rich precursor for CN_x, respectively. To promote the formation of mesopores in the support, an aqueous suspension of silica (3.25 g; Sigma–Aldrich, SiO_2 LUDOX HS-40) was added to the mixture, which was then stirred at 110°C until the complete evaporation of the water phase. The solid product was subsequently calcined in air at 550°C for 4 h, with a heating rate of 2.3°C min^{-1}. After cooling, the powder was dispersed in 50 mL of a 4 M ammonium hydrogen difluoride (NH_4HF_2; Sigma–Aldrich, 95%) solution and stirred at room temperature for 48 h to allow to etch away the silica template. The resulting material was thoroughly washed with Milli-Q water and ethanol under vacuum conditions until a neutral pH was reached, ensuring the complete removal of the etching agent. Finally, the solid powder was dried at 70°C for 16 h to yield the desired catalyst, denoted as $Ni_1@CN_x$, where "1" highlights the monoatomic nature of the metal sites.

2.2 | Oxidation of MWCNT

MWCNT were subjected to mild oxidation following the Hummers method to introduce oxygen-containing functional groups [56], thereby facilitating their interaction with CN_x. Briefly, MWCNT (1 g; Nanocyl NC7000) were calcined in air at 500°C for 1 h with a heating rate of 5°C min^{-1}. The resulting material (300 mg) was washed with a hydrochloric acid solution (HCl; 25 mL; Sigma–Aldrich, 10%) and Milli-Q water (50 mL), then dried at 75°C for 10 min. To activate the material, concentrated sulfuric acid (H_2SO_4; 10 mL; Sigma–Aldrich, 97%) was added dropwise, and the activation reaction was conducted overnight (ca. 18 h) under continuous stirring at room temperature. Sodium nitrate ($NaNO_3$; 100 mg; Sigma–Aldrich, 99%) and potassium permanganate ($KMnO_4$; 300 mg; Sigma–Aldrich, 99%) were introduced, and the reaction mixture was stirred 40°C for 30 min.

To overcome the high viscosity of the solution, which hindered uniform mixing, 1 mL of Milli-Q water was initially added, followed by successive 1 mL aliquots every 5 min until a total volume of 15 mL was reached. The mixture was stirred at 40°C for 15 min and, upon completion of the oxidation process, it was allowed to cool to room temperature. The oxidation process was quenched by the dropwise addition of a hydrogen peroxide (H_2O_2; 3 mL; Sigma–Aldrich, 30%) solution. The resulting oxidized MWCNT (ox-MWCNT) were filtered in 7-mL aliquots to ensure complete removal of oxidative reagents and then thoroughly washed with 5% HCl solution (5 mL per aliquot) and Milli-Q water (3 mL per aliquot).

2.3 | Preparation of Standalone Electrode Films Incorporating Ni SAC and MWCNT

$Ni_1@CN_x$ (5 mg) and MWCNT (5 mg) were added to a Milli-Q water/isopropanol solution (2 mL, 60:40 v/v), and the resulting dispersion was sonicated for 10 min using an ultrasonication probe (120 W, 30 pulse s^{-1}, 30% amplitude). The mixture was transferred to a stainless-steel autoclave lined with polytetrafluoroethylene (PTFE) and subjected to a solvothermal treatment at 120°C for 48 h with a heating rate of 2°C min^{-1}. *N,N*-dimethylformamide (DMF; 33 mL; Carlo Erba, 99%) was added to the mixture, and the obtained solution was sonicated in a sonication bath at room temperature for 2 h (580 W; 100%). Finally, the dispersion was filtered under vacuum through a Millipore filtration system using a PTFE membrane (0.45 µm, 25 mm, hydrophilic) and thoroughly washed with Milli-Q water and acetone. The as-obtained thin film was dried at room temperature for ca. 18 h and denoted as $Ni_1@CN_x$/MWCNT. To prepare metal-free films, the same procedure was followed, excluding the addition of the Ni SAC at the beginning of the synthesis protocol. The dried films composed of either ox-MWCNT or $Ni_1@CN_x$/MWCNT were then cut into 1 × 1.5 cm pieces with a precision cutter and mounted onto a steel rod using copper tape to yield the final electrodes. Additional Parafilm and Teflon tape were applied to isolate the steel support from the electrolyte solution during the electrochemical tests of the electrodes.

2.4 | Characterization of Ni SAC and Standalone Electrode Films

The structural and physicochemical properties of the prepared materials, i.e., $Ni_1@CN_x$, ox-MWCNT, and $Ni_1@CN_x$/MWCNT, were systematically investigated using an extensive array of characterization approaches, including both spectroscopic and microscopic methods. The Ni content in $Ni_1@CN_x$ and $Ni_1@CN_x$/MWCNT was quantified via inductively coupled plasma optical emission spectroscopy (ICP-OES) using a Perkin Elmer Optima 8300 instrument equipped with a photomultiplier tube detector. The analysis involved the dissolution of the material in a strong acidic medium, followed by nebulization to generate a fine aerosol. Excited atoms and ions were produced in an inductively coupled plasma torch, emitting photons at characteristic wavelengths, allowing for the identification and quantification of Ni. The C, N, and H content in the materials was determined through combustion analysis using a Vario MICRO Elemental Analyzer. The samples underwent high-temperature treatment, resulting in their complete combustion, and the gaseous products were separated via gas chromatography and quantified with a thermal conductivity detector. The specific surface areas were calculated resorting to the Brunauer–Emmett–Teller (BET) method applied to the adsorption branch of the N_2 physisorption isotherms within the relative pressure range of $0.05 < p/p_0 < 0.30$, which corresponds to the transition from monolayer to multilayer adsorption of N_2 on their surfaces. X-ray diffraction (XRD) patterns were recorded using a Bruker D2 Phaser X-ray diffractometer equipped with a Cu $K\alpha$ radiation source ($\lambda = 1.54$ Å) in the 10°–50° 2θ range, with a step size of 0.016° and a counting time of 0.4 s $step^{-1}$. Attenuated total reflectance-Fourier transform infrared (ATR-FTIR) spectroscopy measurements were performed with a Smart iTX accessory for ATR mounted on a Thermo Scientific Nicolet iS20 FTIR Spectrometer equipped with a DTGS detector. A total of 128 scans were acquired at a 4 cm^{-1} resolution and then averaged to produce the final infrared spectrum in the 4000–700 cm^{-1} range. High-resolution X-ray photoelectron spectroscopy (XPS) measurements were conducted on a PHI 5000 Versa Probe II XPS system (Physical Electronics), using a monochromatic Al $K\alpha$ source (15 kV, 50 W) with a photon energy of 1486.7 eV. Dual-beam charge compensation was employed for all XPS measurements, and spectra were collected under vacuum conditions (residual pressure $< 1.3 \times 10^{-7}$ Pa). Binding energy values were referenced to the C 1*s* peak located at 284.80 eV, employed as a consistent reference for calibrating the XPS spectra [57]. Scanning electron microscopy (SEM) images were acquired on a HRSEM JEOL JSM-7500LA microscope, equipped with a cold field-emission gun (FEG) and operating at acceleration voltage of 15 kV. The elemental composition of the samples was determined by energy-dispersive spectroscopy (EDS) using an Oxford EDS X-Max detector (80 mm^2) as part of the SEM equipment, with a working distance of 8 mm, acceleration voltage of 15 kV, and 15 sweep counts. Transmission electron microscopy (TEM) micrographs were collected with a JEOL JEM 1011 transmission electron microscope operating at an acceleration voltage of 100 kV. High-resolution scanning transmission electron microscopy (STEM) images were acquired on a probe-corrected Thermo Fisher Spectra 30-300 S/TEM operated at 80 kV. The high resolution images were acquired with a high-angle annular dark field (HAADF) detector, utilizing a current of 40 pA and a beam convergence semiangle of 27 mrad. Compositional maps were acquired using Velox, with a probe current of ~150 pA and rapid rastered scanning by the Energy-Dispersive X-Ray (EDX) spectroscopy on a Dual-X setup comprising two detectors on either side of the sample, for a total acquisition solid angle of 1.76 Sr. Ex situ X-ray absorption spectroscopy (XAS) measurements were carried out at the Quick X-ray Absorption and Scattering (QAS) 7-BM beamline of the National Synchrotron Light Source II (NSLS-II), Brookhaven National Laboratory (BNL). Data were collected at the Ni *K* edge in fluorescence mode using a passivated implanted planar silicon (PIPS) detector. For each sample, 30 scans were acquired and merged to enhance the signal-to-noise ratio. Extended X-ray absorption fine structure (EXAFS) fitting for the $Ni_1@CN_x$/MWCNT composite was carried out in *R* space using the Fourier transform EXAFS (FT-EXAFS) spectrum derived from the k^2-weighted $\chi(k)$ function. Performing the fitting in *R* space enabled the exclusion of higher coordination shells, allowing a focused analysis on the first coordination sphere to systematically investigate structural features relevant to the density functional theory (DFT)-optimized models of the Ni centers. Details related to the EXAFS fitting parameters and results are provided in the Supporting Information (Table S4 and Figure S11). Ab initio simulations of the X-ray absorption near-edge structure (XANES) were performed resorting to the finite difference method near edge structure (FDMNES) code to reproduce the Ni K edge XAS experimental spectra. DFT-optimized geometries of a set of seven configurations of the Ni sites named T1-T7 (Figure S12) were used as input structures, and the simulated spectra were then compared with experimental XANES data (Figure S13). Among the architectures tested, T3 and T6 showed the closest agreement with the experimental data; given its superior resemblance to the experimental XAS spectra, structure T3 was selected as the representative model for further discussion in the manuscript.

2.5 | Electrochemical Properties of Standalone Electrode Films

The electrochemical properties of the ox-MWCNT and $Ni_1@CN_x$/MWCNT electrodes were evaluated using a three-electrode cell system consisting of a platinum wire as the counter electrode (CE), one of the standalone thin films as the working electrode (WE), and an Ag/AgCl (3 M KCl) reference electrode (RE) or an $Ag/AgNO_3$ (0.1 M TBATFB in MeCN) pseudo-reference electrode for tests in aqueous or organic solutions, respectively. Electrochemical measurements were conducted using a BioLogic potentiostat VSP 300. Before cyclic voltammetry (CV) and electrochemical impedance spectroscopy (EIS) experiments, the supporting electrolyte was degassed under a N_2 flow for 30 min. To prevent air diffusion into the electrolyte during the experiments, inert atmosphere conditions were maintained throughout the measurements. CV measurements were performed under both aqueous and organic conditions. In aqueous environments, 1 M H_2SO_4 was used as the electrolyte, while in organic conditions, a 0.1 M tetrabutylammonium tetrafluoroborate (TBATFB) solution in acetonitrile (MeCN) served as the supporting electrolyte. To ensure the reliability of the measurements, the pseudo-reference electrode was preconditioned in the same electrolyte prior to use. EIS measurements were performed using the same three-electrode configuration employed for the CV experiments, with a 1 M H_2SO_4 aqueous solution previously degassed under N_2 flow for 30 min. Prior to data acquisition, the electrodes were conditioned at the open-circuit potential (OCP) of $Ni_1@CN_x$/MWCNT or ox-MWCNT (−0.24 V and +0.25 V, respectively) for 2 min to ensure a stable electrochemical interface. The impedance spectra were then recorded over a frequency interval ranging from 100 kHz to 10 mHz, applying a small sinusoidal amplitude wave of 10 mV to minimize non-linear effects. To accurately describe complex electrode-electrolyte interfaces, the thin electrode films were modeled through an electrical equivalent circuit (EEC), where each component corresponds to a specific electrochemical process occurring at their interface [58]. Experimental impedance data were fitted using a randomized minimization algorithm, followed by parameter refinement via a modified Levenberg–Marquardt algorithm to accurately determine circuit component values, employing the Biologic EC-Lab software.

3 | Results and Discussion

3.1 | Fabrication of Standalone Electrode Films

For the preparation of $Ni_1@CN_x$/MWCNT, the two components ($Ni_1@CN_x$ and ox-MWCNT) were synthesized independently and subsequently combined to form the composite material (refer to "Materials and Methods" for details). $Ni_1@CN_x$ was produced using a hard template-assisted polymerization method, following a well-established protocol reported in the literature [54, 55]. This procedure enabled the synthesis of CN_x-based SAC with a Ni content >2 wt.% while preserving the mesoporous structure inherent to the metal-free CN_x framework, facilitated by the use of SiO_2 nanoparticles as a hard template (Table S1). Given the limitations of CN_x as support material for electrochemical applications, primarily due to its low electrical conductivity [59], the Ni SAC was integrated into a MWCNT matrix via a solvothermal process, thereby enhancing charge transport and overall electrochemical activity. Commercially available MWCNT were functionalized using a modified Hummers method to introduce oxygen-containing functionalities onto the outer walls of the nanotubes. Following a calcination step to remove potential impurities from the as-purchased MWCNT, the material was activated through strong acid treatment and subsequent functionalization with oxidative agents, thus obtaining the ox-MWCNT. $Ni_1@CN_x$/MWCNT was then prepared via a straightforward solvothermal approach, yielding a composite material with a Ni content of ca. 1 wt.% (Table S1).

ICP-OES analysis and STEM imaging coupled with EDS mapping revealed the presence of crystalline alumina (Al_2O_3) particles in the as-purchased MWCNT (Figure 1a), with an initial Al content of 4.45 wt.% (Table S2, Entry 1). Nonetheless, following calcination at 500°C to remove volatile impurities, the Al content increased slightly to 4.99 wt.% (Table S2, Entry 2), likely due to the marginal removal of carbonaceous residues and consequent enrichment of inorganic species. Oxidation of MWCNT via the Hummers method contributed to a marked reduction in Al content to 0.92 wt.% (Table S2, Entry 3). To further decrease the Al impurities, additional purification strategies were systematically tested at the end of the Hummers protocol on ox-MWCNT, including base washing and extended post-oxidation filtration steps (further details provided in the Supporting Information). In particular, for the base-washing protocol, two approaches were compared, consisting of the treatment with an aqueous inorganic base solution (0.1 M $NaHCO_3$) or with an organic base (pyridine). ICP-OES analysis of the resulting ox-MWCNT revealed that the inorganic $NaHCO_3$ wash proved more effective, lowering the Al content to 0.11 wt.% (Table S2, Entry 4), whereas pyridine treatment achieved a less pronounced reduction to 0.46 wt.% (Table S2, Entry 5). Although Al_2O_3 has found applications as a support in heterogeneous catalysis [60], its presence was minimized to ensure that the electrochemical performance of the composite films could be primarily attributed to the Ni SAC and MWCNT components rather than to any Al-derived impurities. Importantly, in all electrochemical measurements, the $Ni_1@CN_x$/MWCNT composite was quantitatively compared to ox-MWCNT, both synthesized using the base-wash-modified Hummers protocol, thereby ensuring that the Al content was

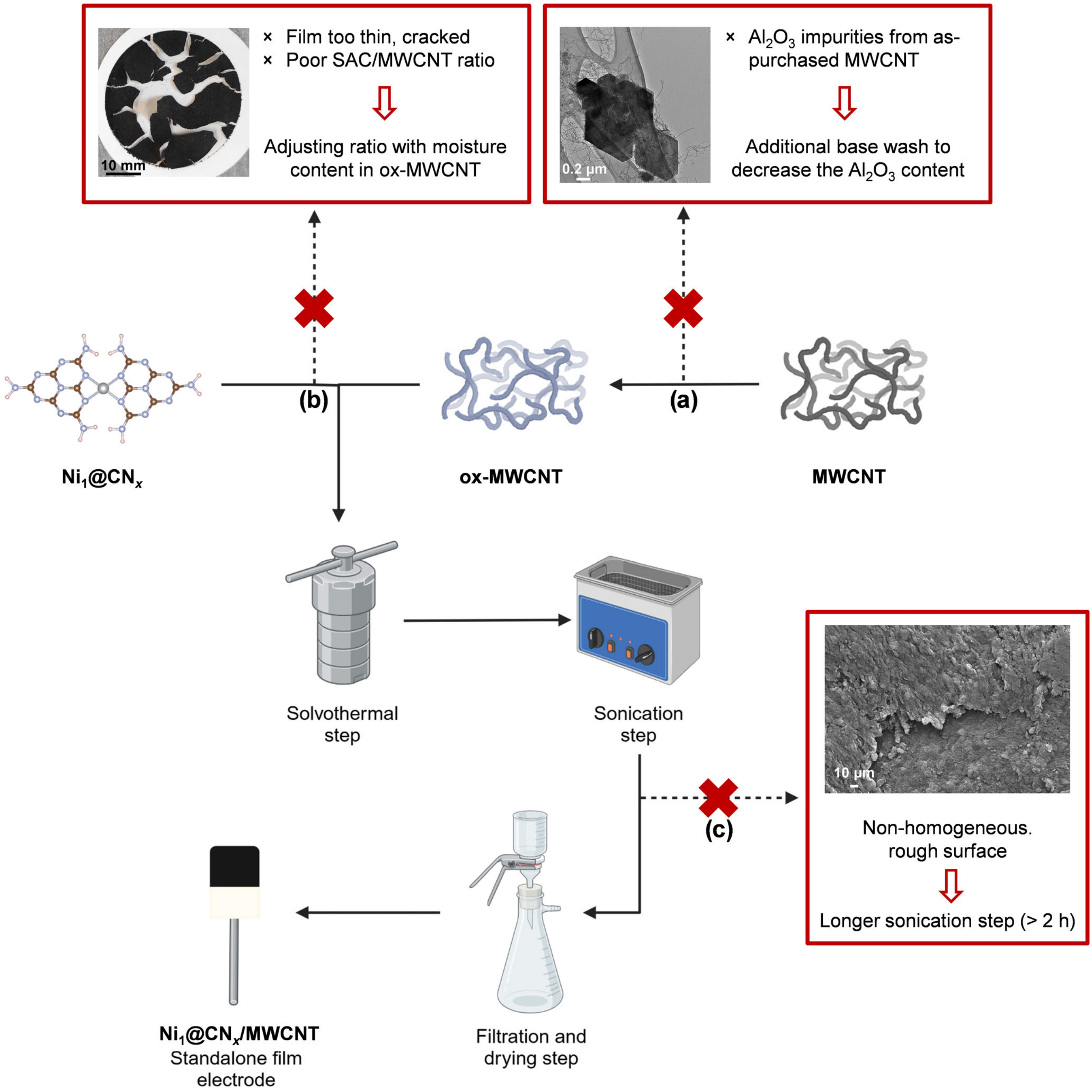

FIGURE 1 | Schematic representation of the Ni SAC-based thin film preparation. TEM image of ox-MWCNT showing Al_2O_3 crystalline impurities (a). Picture of a cracked $Ni_1@CN_x$/MWCNT film (b). SEM image displaying surface non-uniformity in a $Ni_1@CN_x$/MWCNT film (c).

minimized across all samples and did not bias the follow-up analyses.

Following the independent synthesis of ox-MWCNT and $Ni_1@CN_x$, the components were sonicated in a water/isopropanol mixture and subjected to solvothermal treatment, followed by vacuum filtration to yield the $Ni_1@CN_x$/MWCNT composite. Initial attempts to fabricate the electrode films encountered several challenges: the films exhibited non-homogeneous surfaces, were excessively thin, and lacked sufficient mechanical integrity for handling. Additionally, they were also prone to cracking and curling, rendering them unsuitable for experimental use (Figure S1). To address these issues, key parameters in the composite fabrication—namely, the moisture content of the MWCNT and the Ni SAC/MWCNT ratio in $Ni_1@CN_x$/MWCNT—were optimized. The moisture content in ox-MWCNT after the final filtration step was assessed by drying ca. 70 mg of material in a muffle furnace at 70°C for 20 h until constant weight was achieved, resulting in a mass loss of approximately 88% (Table S3). Films prepared using either wet or dried ox-MWCNT showed no significant differences, indicating that time-consuming drying steps may be unnecessary. Therefore, the Ni SAC/MWCNT ratio in $Ni_1@CN_x$/MWCNT required careful optimization to prevent the formation of excessively thin, fragile films prone to cracking during handling or electrode fabrication (Figure 1b). Systematic experiments on the preparation of 16.5

mm diameter films demonstrated that a mass of ca. 8 mg, corresponding to a thickness of 0.07 mm, enabled us to achieve an optimal balance of mechanical robustness, flexibility, and durability. Sonication of the mixture following the solvothermal treatment was also critical to film quality and morphology. Extended sonication times (>2 h) improved surface homogeneity by reducing roughness and eliminating particle agglomeration (Figure 1c). Ultrasonication in an polar aprotic solvent is widely recognized as an effective strategy to promote uniform dispersion of MWCNT-containing dispersions, preventing the formation of bundles, nodes, or agglomerates. DMF, in particular, has been identified as an efficient dispersant for CNTs processing owing to its high electron-pair donicity and solvochromic parameter, along with a negligible hydrogen-bond donating capability. The combination of the solvent properties with strong ultrasonication can effectively overcome the strong van der Waals interactions between the individual CNTs, preventing their agglomeration and resulting in highly homogeneous dispersions [61–63]. Resorting to the optimized preparation protocol, the production of composite electrodes was successfully scaled up, yielding films with diameters ranging from 16.5 to 35.5 mm (Figure S2) with consistent Ni loading (0.94 ± 0.05 wt.%), confirming reproducibility across batches while maintaining the desired mechanical properties of strength and flexibility. The thin films were then cut into 1 × 1.5 cm pieces to fabricate standalone electrodes, with a steel rod serving as the holder and copper tape applied to ensure electrical contact between the film and the rod (Figure S3c).

3.2 | Characterization of $Ni_1@CN_x$, ox-MWCNT, and $Ni_1@CN_x$/MWCNT Composite

The elemental composition and textural properties of $Ni_1@CN_x$, ox-MWCNT, and $Ni_1@CN_x$/MWCNT are summarized in Table S1. The specific surface area of these materials was determined by applying the BET method to the adsorption branch of their N_2 physisorption isotherms (Figure S4). $Ni_1@CN_x$/MWCNT exhibited a surface area greater than that of the Ni SAC but lower than that of the functionalized ox-MWCNT, consistent with the composite nature comprising both $Ni_1@CN_x$ and ox-MWCNT constituents. The pore size distribution of $Ni_1@CN_x$ is centered at ca. 6 nm, whereas both ox-MWCNT and the composite material display smaller yet comparable pore diameters. During the synthesis of $Ni_1@CN_x$/MWCNT, particularly the solvothermal process, partial blocking or alterations of the pores may occur. In fact, interactions between the composite's constituents can alter the overall pore architecture, with the larger pores of $Ni_1@CN_x$ potentially being partially obstructed by MWCNT or their functional groups. Consequently, the pore size distribution of the composite tended to shift toward smaller pore sizes and does not represent a simple average of the individual components. The structural properties and chemical environments of $Ni_1@CN_x$/MWCNT, as revealed by XRD patterns and ATR-FTIR spectra, were consistent with those of the two main components. In the infrared spectra of $Ni_1@CN_x$ and the composite (Figure S5), infrared signals in the 1100–1700 cm^{-1} region were assigned to the stretching modes of aromatic C–N heterocycles, while the sharp peak at ~805 cm^{-1} corresponded to the characteristic breathing mode of the aromatic repeating units forming the CN_x framework. A broad band between 3000 and 3500 cm^{-1} was attributed mainly to N–H stretching vibrations associated to uncondensed amine moieties arising from residual amino groups at the edges of the heterocycles [54, 64]. In the ATR-FTIR spectra of the functionalized MWCNT, a broad band centered at ~3450 cm^{-1} together with a feature localized at ~1630 cm^{-1} were attributed to the presence of O–H groups, confirming the oxidized nature of the nanotubes. Additional infrared peaks at slightly higher and lower frequencies were consistent with oxidic surface groups, in agreement with the successful oxidation of the MWCNT by the Hummers method. Furthermore, a broad band around 3000 cm^{-1} was attributed to C–H_x stretching, typical of carbon matrices such as CNTs. Although the overlapping of $Ni_1@CN_x$ and ox-MWCNT features made the recognition of individual peaks more challenging in the composite, the detection of characteristic bands from both components, including the broad signal in the 3000–3500 cm^{-1} region, confirmed the successful integration of the two materials in the thin-films [65, 66]. Phase purity and crystallinity of $Ni_1@CN_x$, ox-MWCNT, and their composite were further examined by powder XRD (Figure S6). In the pattern of ox-MWCNT, the strong reflection at $2\theta = 26°$ was assigned to the (002) plane, corresponding to the interlayer spacing of graphitic-like planes, while the weaker reflection at 43° was indexed to the (100) reflection arising from the in-plane periodicity of C atoms in the hexagonal lattice [67]. In contrast, $Ni_1@CN_x$ displayed two broad reflections at $2\theta = 13°$ and 27°, attributed to the (100) and (002) planes of the CN_x framework, respectively. The weak intensity of the (100) reflection indicated the in-plane structural packing motif of the aromatic units, whereas the (002) reflection was associated with interlayer stacking of graphitic-like CN_x sheets [54]. Importantly, no additional peaks attributable to other phases or Ni nanoparticles were observed, confirming the absence of major crystalline impurities. The detection of reflection planes characteristic of both $Ni_1@CN_x$ and ox-MWCNT in the diffractogram of the $Ni_1@CN_x$/MWCNT composite further corroborated the successful integration of the two materials.

HR-STEM micrographs were collected to rule out the potential presence of crystalline impurities or metal clusters originating from the aggregation of Ni atoms in the $Ni_1@CN_x$/MWCNT composite. The HAADF-STEM image of $Ni_1@CN_x$/MWCNT shown in Figure 2a,c confirmed the absence of major crystalline phases and metal nanoparticles. At lower magnifications, TEM images revealed that the $Ni_1@CN_x$ particles, with sizes ranging from 50 to 200 nm, served as adhesive agents, effectively connecting multiple MWCNT of the carbonaceous framework simultaneously (Figure S7). EDS mapping of $Ni_1@CN_x$/MWCNT (Figure 2c–e) provided supportive evidence of the spatial distribution of elements in the composite. In agreement with our spectroscopic analyses (vide infra), the Ni and N signals were localized within the CN_x particles, which are embedded in and interacting with the CNT matrix, where carbon remains predominant. Complementary SEM-EDS mapping on the $Ni_1@CN_x$/MWCNT film (Figure S8) further confirmed that Ni is homogeneously dispersed and confined to the CN_x domains of the composite. Additional STEM and SEM imaging and EDS acquisitions were conducted on the composite following its use as a working electrode in CV measurements (Figure S9). The acquired micrographs confirmed the robustness and structural integrity of the thin film, as no significant changes in metal content or element distribution were detected after electrochemical testing. As shown in

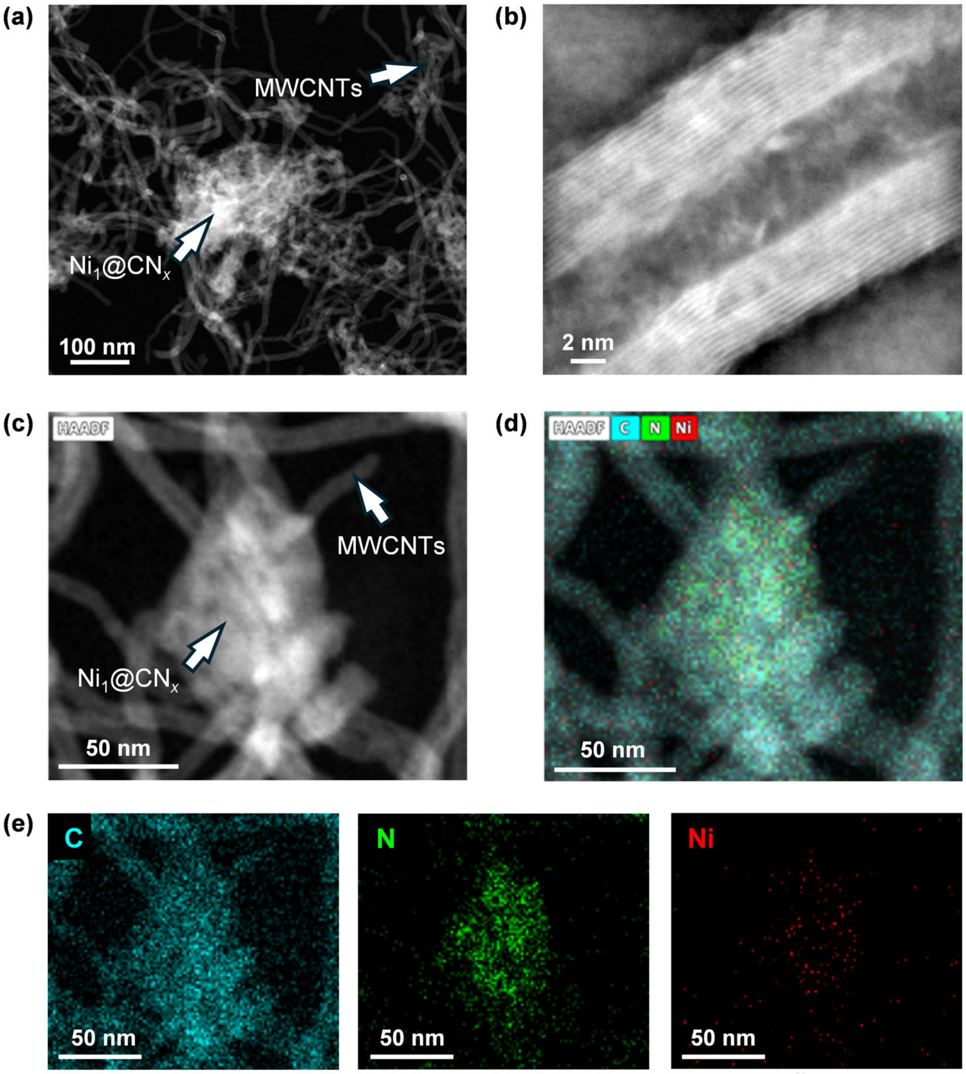

FIGURE 2 | HAADF-STEM image of Ni$_1$@CN$_x$/MWCNT (a) and ox-MWCNT (b). HAADF-STEM image of Ni$_1$@CN$_x$/MWCNT (c) and corresponding EDS elemental maps showing the spatial distribution of C (blue), N (green), and Ni (red) (d,e).

Figure S10, only a slight increase in the surface roughness was observed, together with entrapment of residual solvent within the interstitial spaces between the dense MWCNT network.

To further validate the atomically dispersed nature of Ni species in Ni$_1$@CN$_x$/MWCNT and probe the electronic properties and coordination environment of the Ni centers, XAS measurements were conducted on Ni$_1$@CN$_x$ and Ni$_1$@CN$_x$/MWCNT. Reference spectra for NiO and Ni metal foil were also collected and used as benchmarks in the subsequent data analysis. As shown in the Ni *K* edge XANES spectra displayed in Figure 3a, clear differences were observed between the samples and reference compounds, indicating distinct electronic environments around the Ni atoms. The FT-EXAFS spectra (Figure 3b) further revealed that the first-shell scattering contributions for Ni$_1$@CN$_x$ and Ni$_1$@CN$_x$/MWCNT occur at significantly shorter radial distances than those in NiO, consistent with a Ni—N coordination rather than Ni—O or Ni—Ni bonding.

To evaluate the potential presence of undesired Ni—Ni interactions in the composite, quantitative EXAFS fitting was conducted using a non-linear least squares approach via the Artemis software [68]. The theoretical fitting procedure accounted for both Ni—N and Ni—Ni scattering paths for the excited photoelectrons, allowing for variations in coordination numbers of the Ni site, bond lengths, and Debye-Waller factors. The resulting fits for Ni$_1$@CN$_x$/MWCNT (Table S4 and Figure S11) indicated that the local environment of Ni is best described by Ni—N bonding systems, with a coordination number of 4.7 ± 0.8. Notably, the inclusion of a Ni—Ni path did not improve the fit quality, further confirming the absence of metallic Ni clustering.

The EXAFS-derived structural parameters were compared with seven plausible geometries of the Ni site obtained from DFT-optimized models (Figure S12), all of which exhibited average Ni—N bond lengths consistent with the experimental value of 1.86 ± 0.01 Å. To further assess these candidate architectures, Ni *K* edge XANES simulations were carried out using the FDMNES code [69], and the resulting theoretical spectra were benchmarked with spectroscopic outputs (Figure S13). As shown in Figure 3c, among the tested models, structure T3 showed the closest agreement with the experimental XANES spectrum,

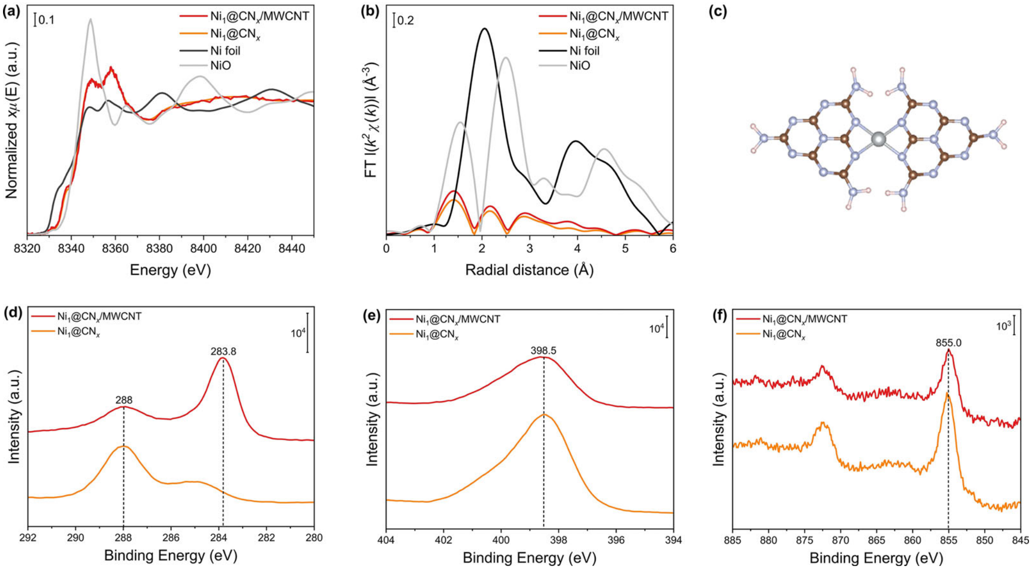

FIGURE 3 | Ni K edge XANES spectra (a) and k^2-weighted FT-EXAFS spectra (b) of Ni$_1$@CN$_x$/MWCNT and Ni$_1$@CN$_x$, compared with Ni metal foil and NiO as reference materials. DFT-optimized structural model of the cavity hosting Ni in the Ni$_1$@CN$_x$ and Ni$_1$@CN$_x$/MWCNT composite, showing the best agreement with experimental data and EXAFS fitting (c). XPS spectra of Ni$_1$@CN$_x$/MWCNT and Ni$_1$@CN$_x$ showing (d) C 1s, (e) N 1s, and (f) Ni 2p core-level regions.

successfully reproducing its key spectral features. This supported the assignment of T3 as the most representative local configuration for the Ni sites in both Ni$_1$@CN$_x$ and Ni$_1$@CN$_x$/MWCNT.

To corroborate experimental outcomes from XAS experiments, XPS measurements were conducted to probe the binding state of Ni, C, and N species in the Ni$_1$@CN$_x$/MWCNT composite. The C 1*s* spectrum (Figure 3d) displayed a dominant peak at 283.8 eV, attributed to C═C bonds within the MWCNT structure, along with an additional feature at 288.0 eV, ascribed to *sp*^{2}-bonded C in the heptazine rings of the CN$_x$ matrix [70–72]. The N 1*s* spectrum showed contributions from pyridinic (398.5 eV) and graphitic (399.4 eV) N species, as well as a component at 400.8 eV associated with uncondensed primary or secondary amine groups (Figure 3e) [70–72]. The Ni 2*p* spectrum confirmed the presence of Ni^{2+} species, with no detectable Ni^0 (Figure 3f), thereby indicating that Ni atoms carry a positive charge and that metallic Ni particles are absent, in agreement with recent reports [73].

3.3 | Electrochemical Properties of the Thin-Film Electrodes

The electrochemical performance of the Ni$_1$@CN$_x$/MWCNT and ox-MWCNT electrode films was evaluated by CV in terms of conductivity and stability. Following the characterization of the physicochemical and electronic properties of the novel materials, and the assessment of the single-atom nature of the Ni sites, thin films were cut into 1 × 1.5 cm pieces and fixated to steel rods using copper tape to ensure optimal electrical contact. The standalone electrode films were then employed as the WE in the subsequent electrochemical experiments, in a three-electrode setup, together with a Pt wire as the CE, and an Ag/AgCl or Ag/AgNO$_3$ electrode as the RE or pseudo-RE, respectively. For the electrochemical experiments, Ni$_1$@CN$_x$ powder was deposited on glassy carbon (GC) using NAFION$^{\text{TM}}$ as a binder. The catalyst "ink" was prepared by sonicating 2 mg of Ni SAC in a mixture of ethanol (500 μL) and Milli-Q water (450 μL) with 50 μL of NAFION$^{\text{TM}}$, and subsequently drop-casted onto the surface of a clean GC electrode, followed by drying prior to use. CV curve of the pristine Ni$_1$@CN$_x$ catalyst was recorded in organic conditions (in 0.1 м TBATFB in dry MeCN) over a wide electrochemical window (EW) ranging from +3 to −3 V at a scan rate of 100 mV s^{-1}(Figure 4a). The pristine SAC exhibited irreversible redox processes in the anodic region as well as a reversible process in the cathodic region, achieving low current response (120 to −60 μA). In contrast, while some anodic redox features of the Ni composite remain visible, the CV of the Ni$_1$@CN$_x$/MWCNT composite was dominated by the electrochemical response of the MWCNT component, reaching significantly higher currents (Figure 4b).

To evaluate the conductivity and stability of the as-synthesized electrodes, electrochemical tests were conducted in both aqueous (1 м H$_2$SO$_4$) and organic (0.1 м TBATFB in MeCN) solutions, using one standalone film of Ni$_1$@CN$_x$/MWCNT or ox-MWCNT for each supporting electrolyte. Overall, each film withstood approximately 15 h of continuous electrochemical testing, including OCP, CV, and EIS experiments. Initially, the electrode materials were subjected to CV measurements over an EW ranging from +1 to −1 V (vs Ag/AgNO$_3$) at a scan rate of 100 mV s^{-1} for 100 consecutive cycles. Both materials required ca. 10 cycles to stabilize their electrochemical response, after which no significant alteration was observed. The CV profiles corresponding to the 100th cycle of Ni$_1$@CN$_x$/MWCNT and ox-MWCNT electrodes collected in the organic and inorganic media are presented in Figure 5a,b, respectively. In both cases, noise appeared at the EW limits, mainly ascribed to the standalone nature of the thin films and their potential connection limitations. Nonetheless, the Ni$_1$@CN$_x$/MWCNT electrode exhibited increased stability, with reduced noise in the spectra. This

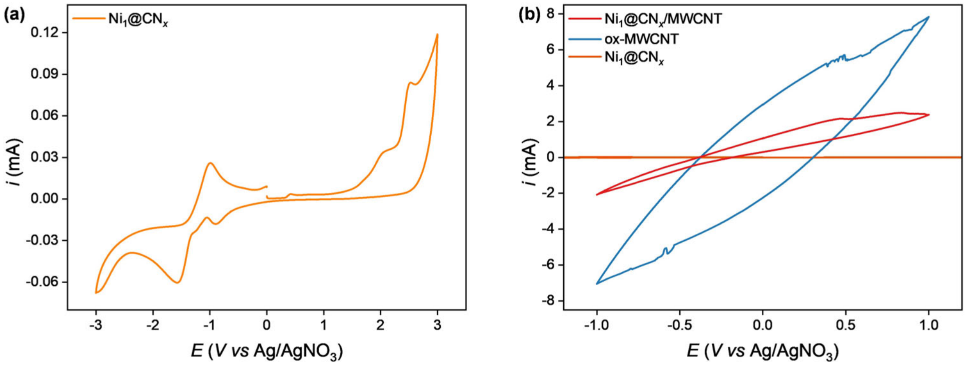

FIGURE 4 | CV curve of the $Ni_1@CN_x$ deposited on GC electrode (a), and pristine $Ni_1@CN_x$ deposited on GC electrode, ox-MWCNT, and $Ni_1@CN_x$/MWCNT thin film electrodes (b) recorded in 0.1 M TBATFB in MeCN at 100 mV s^{-1}.

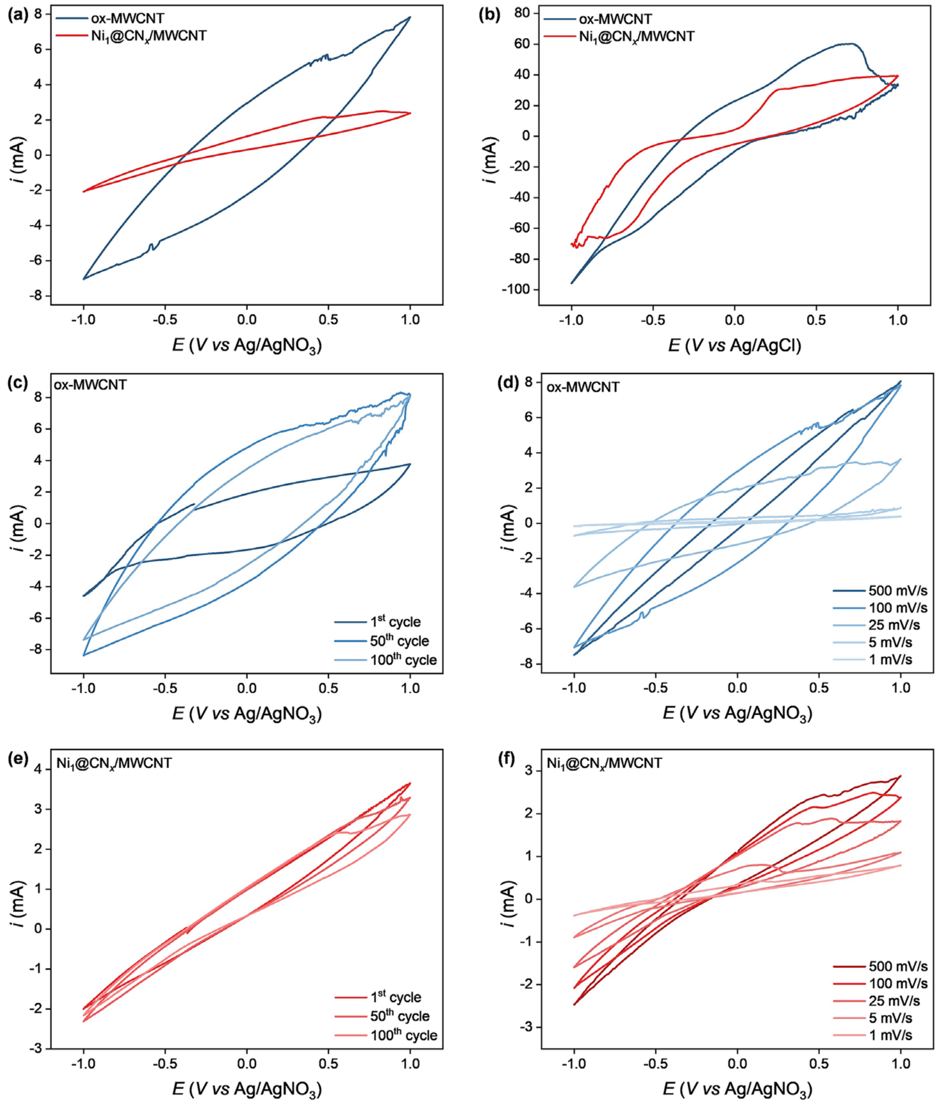

FIGURE 5 | CV curves of the $Ni_1@CN_x$/MWCNT and ox-MWCNT electrodes recorded in 0.1 M TBATFB in MeCN (a) and in 1 M H_2SO_4 aqueous solution (b) at 100 mV s^{-1}. 1st, 50th, and 100th CV scans of the ox-MWCNT films acquired in 0.1 M TBATFB in MeCN at 100 mV s^{-1} (c) and at varying scan rates (d). 1st, 50th, and 100th CV scans of the $Ni_1@CN_x$/MWCNT thin-film electrode collected in 0.1 M TBATFB in MeCN at 100 mV s^{-1} (e) and at varying scan rates (f).

improved electrochemical response of the composite material was attributed to the adhesive-like properties of the $Ni_1@CN_x$ particles to the MWCNT framework (as discussed in section 3.2). An increased current response was recorded in the aqueous environments (60 to −100 mA) compared to the organic media (8 to −7 mA), consistent with the lower solution resistance of the 1 M H_2SO_4 relative to 0.1 M TBATFB in MeCN [74]. In both solutions, the CV curves displayed some degree of hysteresis, a phenomenon commonly arising when the electrochemical system's response to the application of an external load (here, the applied voltage) differs from its response upon reversal of such load [75]. Notably, the bare MWCNT thin film exhibited a significantly higher current response than the Ni-loaded composite (Figure 5a,b), an effect ascribed to the increased surface area of pristine MWCNT (Table S1), while the incorporation of $Ni_1@CN_x$ particles likely induced a reduction in overall conductivity. In the organic electrolyte, the CV curves exhibited a linear increment in current response at increasing scan rate, indicative of charging/discharging effects of the electrical double layer at the electrode-electrolyte interface. These observations suggested that the electrochemical behavior of the electrode films was primarily governed by resistive processes and slow electron transfer kinetics. Despite their difference in electrochemical behavior, $Ni_1@CN_x$/MWCNT and ox-MWCNT electrodes demonstrated exceptional stability across prolonged cycling in both aqueous (Figure S14) and organic conditions (Figure 5c,e). Additional stability tests, performed at scan rates from 500 to 100 mV s^{-1} (10 cycles) and from 50 to 1 mV s^{-1} (5 cycles), further confirmed the mechanical and electrochemical robustness of the standalone electrode films, although minor distortions were observed at higher scan rates (Figure 5d,f). The long-term stability achieved (corresponding to ca. 15 h of continuous cycling) stems from the synergistic interplay between the $Ni–N_4$ coordination environment and the conductive, defect-engineered CNT scaffold, which jointly preserve atomic dispersion and electron transport under electrochemical stress. The result represents an order-of-magnitude improvement over existing binder-free SAC films and establishes a reproducible route from atomic precision to device integration. Moreover, this robustness distinguishes the films from previous binder-free SAC electrodes and serves as a scalable route from powders to functional devices. In addition to the stability study of the materials, a scan rate study was performed to determine whether the observed redox processes observed were adsorption- or diffusion-controlled. This was achieved by plotting the peak current I_p against the scan rates (ν) or the square-root of the scan rate ($\nu^{1/2}$) [76, 77]. For the $Ni_1@CN_x$/MWCNT composite, which exhibited redox processes in the anodic region, only the first observed I_p were considered. A higher degree of linearity of the current intensity was observed when plotting it against $\nu^{1/2}$ ($R^2 = 0.97$), suggesting that diffusion control was dominating the redox process (Figure S15a,b). Despite the ox-MWCNT thin film showing no distinct redox-related features in the CV curves, I_p values were selected based on the potential peak of the Ni composite and plotted for comparative purposes (Figure S15c,d). The resulting non-linear behavior confirmed the presence of more complex and irregular processes occurring at the electrode-electrolyte interface of the bare ox-MWCNT electrode. Overall, the standalone thin films demonstrated robust performance and structural integrity under continuous electrochemical measurements, withstanding ca. 15 h of testing and characterization. The $Ni_1@CN_x$/MWCNT electrode displayed redox activity in the anodic region, with scan rate studies suggesting a diffusion-controlled electrochemical behavior, along with more uniform CV curves, highlighting an increased mechanical and electrochemical stability.

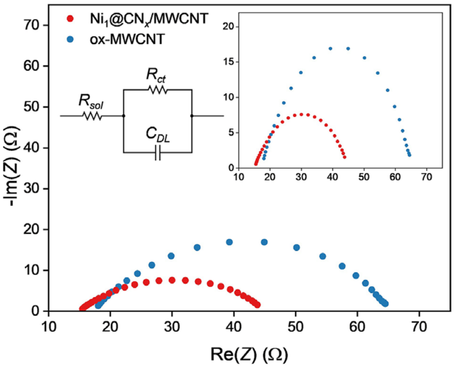

FIGURE 6 | Nyquist plot of the $Ni_1@CN_x$/MWCNT and ox-MWCNT thin films recorded in 1 M H_2SO_4. The inset displays the EEC model proposed for the electrode-electrolyte interface of the electrochemical systems.

To further examine the stability and electrode-electrolyte interface of the $Ni_1@CN_x$/MWCNT and ox-MWCNT thin films, EIS measurements were conducted in the same three-electrode system employed for the acquisition of CV curves, in 1 M H_2SO_4 aqueous solution previously degassed under N_2. The initial impedance spectra displayed a depressed semicircle at high frequencies, transitioning to a linear region with a ~45° slope at low frequencies (10 mHz to 10 Hz), indicative of a Warburg-type diffusion-controlled process at the electrode-electrolyte interface (Figure S16) for the Ni composite film. Based on these observations, subsequent EIS experiments were conducted within a refined frequency range of 10 Hz to 100 kHz to selectively probe the kinetically relevant electrochemical processes. Figure 6 displays representative Nyquist plots obtained from EIS measurements, illustrating the behavior of $Ni_1@CN_x$/MWCNT and ox-MWCNT electrode films in the high-frequency range. The real component of the impedance is plotted on the x-axis, while the imaginary part on the y-axis. Both materials exhibited a depressed semicircle in the complex plane. These results suggested that $Ni_1@CN_x$/MWCNT and ox-MWCNT behave as non-ideal systems, as expected from porous electrodes, with adsorption and diffusion phenomena occurring at the electrode-electrolyte interface [78, 79].

To accurately describe the complex electrode-electrolyte interface, the electrode systems were modeled using the EEC shown as an inset in Figure 6. This model comprises the solution resistance (R_{sol}) in series with the charge transfer resistance (R_{ct}), which is in parallel with a constant phase element (CPE). The inclusion of a CPE, rather than a pure capacitor, accounts for the heterogeneous nature of the electrode surface, and its frequency-dependent impedance can be described by Equation (1) [58]:

$$Z_{CPE} = \frac{1}{(j\omega)^{\alpha} Q_0} \tag{1}$$

TABLE 1 | EEC parameters obtained using randomized minimization algorithm and refinement through the modified Levenberg-Marquardt minimization algorithm.

Entry	Material	R_{sol} (Ω)	R_{ct} (Ω)	Q_0 (mF $s^{\alpha-1}$)	α	C_{DL} (μF)
1	ox-MWCNT film	17.65	47.26	0.028	0.798	21.61
2	Ni_1@CN_x/MWCNT film	14.80	30.50	0.190	0.596	295.45

where Z_{CPE} represents the CPE impedance, ω is the angular frequency, Q_0 is the CPE constant, and α is a parameter ranging from 0 to 1, which determines the phase angle of the CPE. It is important to note that when $\alpha = 1$, the CPE behaves as a pure capacitor, whereas when $\alpha = 0$, the CPE acts as a pure resistor. Based on these considerations, the double-layer capacitance (C_{DL}) can be expressed through Equation (2) [58]:

$$C_{DL} = \left[Q_0 \left(\frac{1}{R_{sol}} + \frac{1}{R_{ct}} \right)^{\alpha - 1} \right]^{1/\alpha} \tag{2}$$

The experimental impedance data were fitted using a randomized minimization algorithm, followed by parameter refinement through the modified Levenberg–Marquardt minimization algorithm to determine the values of the circuit components (Table 1; Figure S17). The fitting results showed that both Ni_1@CN_x/MWCNT and ox-MWCNT are characterized by resistances of comparable order of magnitude. Notably, the Ni_1@CN_x/MWCNT electrode exhibits a slightly lower R_{sol} and a decreased R_{ct}, indicative of faster electron transfer kinetics at the composite electrode-electrolyte interface compared to the ox-MWCNT counterpart. Regarding capacitive behavior, the calculated C_{DL} of Ni_1@CN_x/MWCNT film is significantly higher, suggesting a greater density of accumulated charges at the surface, likely associated to the presence of the Ni single atoms. N_2 physisorption measurements (Table S1) revealed that the bare ox-MWCNT films is characterized by a greater surface area (357.61 m^2 g^{-1}) than the Ni composite films (164.17 m^2 g^{-1}), therefore indicating that the enhanced C_{DL} of Ni_1@CN_x/MWCNT cannot be attributed solely to differences in accessible surface area, but rather to the specific role of Ni single atoms in modulating the electrochemical interface. Comparative analyses with MWCNT-based electrodes further demonstrated that integrating the Ni SAC within the ox-MWCNT framework significantly improved electrochemical performance and enhanced electrode stability and robustness beyond the additive contributions of the individual components. This synergistic effect was reflected in the observed substantial decrease in R_{ct} (30.50 Ω) and increase in C_{DL} (295.45 μF). Overall, both materials exhibited resistances in the ohmic range, in agreement with the resistive features observed in CV measurements and EIS spectra, as well as moderate capacitance values in the μF range. The resistive properties of Ni_1@CN_x/MWCNT and ox-MWCNT, especially their relatively high R_{ct}, suggested a notable barrier to electron transfer, which may limit their applicability in systems requiring fast charge transport, such as high-power batteries, electrocatalysis, or fuel cells. Nevertheless, for potential biosensing applications, the coexistence of resistive and capacitive behavior can be advantageous. More specifically, improved R_{ct} values may serve as intrinsic filtering mechanisms that enhance the selectivity in the detection and quantification of target analytes, while moderate C_{DL} provides a stable background current [80].

4 | Conclusions

In summary, we have developed a straightforward and reproducible approach for fabricating binder-free, standalone thin-film electrodes composed of MWCNT and CN_x-supported Ni SACs. Extensive characterization of the composite materials was performed using a variety of spectroscopic and microscopic techniques, confirming the successful incorporation of the Ni isolated centres within the electrodes. The resulting Ni_1@CN_x/MWCNT thin films exhibited strong mechanical and chemical stability, enabling prolonged electrochemical measurements. Specifically, electrochemical properties, evaluated via CV and EIS in a three-electrode setup with the novel films as the working electrode, revealed excellent stability over multiple cycles, a wide electrochemical window, and consistent performance across varying scan rates in both aqueous and organic media. The integration of Ni SACs within MWCNT significantly impacted the electrochemical performance beyond the contribution of the individual components, as reflected by an increased C_{DL} (295.45 μF) and reduced R_{ct} (30.50 Ω), highlighting the synergistic effect and the role of Ni single atoms in improving the charge transfer properties of the novel materials. This combination of resistive and capacitive behavior, along with the robustness and scalability of these thin-film electrodes, holds significant promise for real-world electrochemical sensing applications, including enzyme-free glucose detection, biomarker analysis, and wearable diagnostic platforms, where prolonged stability and reproducibility are essential. Beyond sensing, this approach establishes a scalable route to robust, single-atom–based electrodes for energy conversion technologies. Future work will focus on *operando* spectroscopic validation of the Ni–N_4 stability during long-term cycling to further elucidate the origin of observed robustness.

Acknowledgements

M.V. and N.A. acknowledge funding from the Horizon Europe's "Global Challenges and European Industrial Competitiveness" programme of the European Commission (grant agreement 101057430, SusPharma). G.V. thanks the European Research Council for financial support (grant agreement 101075832, SAC_2.0). A.I.F. acknowledges support by the U. S. National Science Foundation under grant 2452446. This research used beamlines 7-BM (Quick X-ray Absorption and Scattering, QAS) of the National Synchrotron Light Source II, a Department of Energy (DOE) Office of Science User Facility operated by Brookhaven National Laboratory under Contract DE-SC0012704. Beamline operations were supported in part by the Synchrotron Catalysis Consortium (DOE Office of Basic Energy Sciences Grant DE-SC0012335). Dr. Mark A. Bajada (Politecnico di Milano) is thanked for technical support.

Open access publishing facilitated by Politecnico di Milano, as part of the Wiley - CRUI-CARE agreement.

Conflicts of Interest

The authors declare no conflicts of interest.

Data Availability Statement

The data that support the findings of this study are available from the corresponding author upon reasonable request.

References

1. P. C. Sherrell, M. Iesalnieks, Y. Ehrnst, A. R. Rezk, and A. Šutka, “Electrocatalysis for Green(Er) Chemistry: Limitations and Opportunities with Traditional and Emerging Characterization Methods for Tangible Societal Impact,” *Advanced Energy and Sustainability Research* 5 (2024): 2400008.

2. M. A. Bajada, J. Sanjosé-Orduna, G. Di Liberto, et al., “Interfacing Single-Atom Catalysis with Continuous-Flow Organic Electrosynthesis,” *Chemical Society Reviews* 51 (2022): 3898–3925.

3. P. Anastas and N. Eghbali, “Green Chemistry: Principles and Practice,” *Chemical Society Reviews* 39 (2010): 301–312.

4. E. J. Horn, B. R. Rosen, and P. S. Baran, “Synthetic Organic Electrochemistry: an Enabling and Innately Sustainable Method,” *ACS Central Science J* 2 (2016): 302–308.

5. M. Regnier, C. Vega, D. I. Ioannou, and T. Noël, “Enhancing Electrochemical Reactions in Organic Synthesis: the Impact of Flow Chemistry,” *Chemical Society Reviews* 53 (2024): 10741–10760.

6. Y. Sun, J. Miao, X. Fan, K. Zhang, and T. Zhang, “Recent Progress in Electrochemical Conversion from Biomass Derivatives into High-Value-Added Chemicals,” *Small Structures* 5 (2024): 2300576.

7. D. S. Mallapragada, Y. Dvorkin, M. A. Modestino, et al., “Decarbonization of the Chemical Industry through Electrification: Barriers and Opportunities,” *Joule* 7 (2023): 23–41.

8. L. F. T. Novaes, J. Liu, Y. Shen, L. Lu, J. M. Meinhardt, and S. Lin, “Electrocatalysis as an Enabling Technology for Organic Synthesis,” *Chemical Society Reviews* 50 (2021): 7941–8002.

9. M. J. Orella, Y. Román-Leshkov, and F. R. Brushett, “Emerging Opportunities for Electrochemical Processing to Enable Sustainable Chemical Manufacturing,” *Current Opinion in Chemical Engineering* 20 (2018): 159–167.

10. N. Kaeffer and W. Leitner, “Electrocatalysis with Molecular Transition-Metal Complexes for Reductive Organic Synthesis,” *JACS Au* 2 (2022): 1266–1289.

11. C. Zhu, N. W. J. Ang, T. H. Meyer, Y. Qiu, and L. Ackermann, “Organic Electrochemistry: Molecular Syntheses with Potential,” *ACS Central Science J* 7 (2021): 415–431.

12. S. B. Beil, D. Pollok, and S. R. Waldvogel, “Reproducibility in Electroorganic Synthesis—Myths and Misunderstandings,” *Angewandte Chemie, International Edition* 60 (2021): 14750–14759.

13. G. Smith and E. J. F. E. Dickinson, “Reproducibility and Uncertainty in Experiments for Electrochemical Energy Technologies,” *Nature Communications* 13 (2022): 6832.

14. N. Elgrishi, K. J. Rountree, B. D. McCarthy, E. S. Rountree, T. T. Eisenhart, and J. L. Dempsey, “A Practical Beginner’s Guide to Cyclic Voltammetry,” *Journal of Chemical Education* 95 (2018): 197–206.

15. C. Kingston, M. D. Palkowitz, Y. Takahira, et al., “A Survival Guide for the ″Electro-Curious,” *Accounts of Chemical Research* 53 (2020): 72–83.

16. T. Asefa, C. Tang, and M. Ramírez-Hernández, “Nanostructured Carbon Electrocatalysts for Energy Conversions,” *Small* 17 (2021): 2007136.

17. J. L. Figueiredo, “Application of Nanocarbon Materials to Catalysis,” *Nanotechnology in Catalysis* (Wiley, 2017): 37–56.

18. A. Wang, J. Li, and T. Zhang, “Heterogeneous Single-Atom Catalysis,” *Nature Reviews Chemistry* 2 (2018): 65–81.

19. G. Vilé, D. Albani, M. Nachtegaal, et al., “A Stable Single-Site Palladium Catalyst for Hydrogenations,” *Angewandte Chemie, International Edition* 54 (2015): 11265–11269.

20. M. A. Bajada, M. Tschulkow, and G. Vilé, “Sustainability Assessment of Single-Atom Catalysts in the Transition to Greener Chemical Processes,” *Cell Reports Sustainability* 2 (2025): 100286.

21. V. B. Saptal, V. Ruta, M. A. Bajada, and G. Vilé, “Single-Atom Catalysis in Organic Synthesis,” *Angewandte Chemie, International Edition* 62 (2023): 202219306.

22. M. Melchionna and P. Fornasiero, “On the Tracks to “Smart” Single-Atom Catalysts,” *Journal of American Chemical Society* 147 (2025): 2275–2290.

23. A. Bakandritsos, R. G. Kadam, P. Kumar, et al., “Mixed-Valence Single-Atom Catalyst Derived from Functionalized Graphene,” *Advanced Materials* 31 (2019): 1900323.

24. M. B. Gawande, P. Fornasiero, and R. Zbořil, “Carbon-Based Single-Atom Catalysts for Advanced Applications,” *ACS Catalysis* 10 (2020): 2231–2259.

25. J. Luo, H. Chand, R. Luque, A. M. Balu, and G. Vilé, “Structured, Shaped, or Printed Single-Atom Catalysts and Their Applications,” *Advanced Functional Materials* 35 (2025): 2424514.

26. G. Yasin, S. Ali, S. Ibraheem, et al., “Simultaneously Engineering the Synergistic-Effects and Coordination-Environment of Dual-Single-Atomic Iron/Cobalt-sites as a Bifunctional Oxygen Electrocatalyst for Rechargeable Zinc-Air Batteries,” *ACS Catalysis* 13 (2023): 2313–2325.

27. S. Büchele, A. Yakimov, S. M. Collins, et al., “Elucidation of Metal Local Environments in Single-Atom Catalysts Based on Carbon Nitrides,” *Small* 18 (2022): 2202080.

28. P. Song, M. Luo, X. Liu, et al., “Zn Single-Atom Catalyst for Highly Efficient Oxygen Reduction Reaction,” *Advanced Functional Materials* 27 (2017): 1700802.

29. H. Tian, A. Song, P. Zhang, et al., “High Durability of Fe–N–C Single-Atom Catalysts with Carbon Vacancies toward the Oxygen Reduction Reaction in Alkaline Media,” *Advanced Materials* 35 (2023): 2210714.

30. P. Kumar, K. Kannimuthu, A. Shayesteh Zeraati, et al., “High-Density Cobalt Single-Atom Catalysts for Enhanced Oxygen Evolution Reaction,” *Journal of American Chemical Society* 145 (2023): 8052–8063.

31. L. Hu, C. Dai, L. Chen, et al., “Metal-Triazolate-Framework-Derived FeN_4Cl_1 Single-Atom Catalysts with Hierarchical Porosity for the Oxygen Reduction Reaction,” *Angewandte Chemie, International Edition* 60 (2021): 27324–27329.

32. T. Zhang, J. Jin, J. Chen, et al., “Pinpointing the Axial-ligand Effect on Platinum Single-atom Catalysts towards Efficient Alkaline Hydrogen Evolution Reaction,” *Nature Communications* 13 (2022): 6875.

33. R. Qi, B. Zhu, Z. Han, and Y. Gao, “High-Throughput Screening of Stable Single-Atom Catalysts in CO_2 Reduction Reactions,” *ACS Catalysis* 12 (2022): 8269–8278.

34. X. Zhang, Z. Wang, X. Li, et al., “Competitive Electrochemical Sensing for Cancer Cell Evaluation Based on Thionine-Interlinked Signal Probes,” *Analyst* 148 (2023): 912–918.

35. S. Han, W. Liu, M. Zheng, and R. Wang, “Label-Free and Ultrasensitive Electrochemical DNA Biosensor Based on Urchinlike Carbon Nanotube-Gold Nanoparticle Nanoclusters,” *Analytical Chemistry* 92 (2020): 4780–4787.

36. P. Malla, G. Chen, H. Liao, C. Liu, and W. Wu, "Label-Free Parathyroid Hormone Immunosensor Using Nanocomposite Modified Carbon Electrode," *Journal of Electroanalytical Chemistry* 880 (2021): 114917.

37. B. Zhao, J. Liu, C. Xu, et al., "Hollow NiSe Nanocrystals Heterogenized with Carbon Nanotubes for Efficient Electrocatalytic Methanol Upgrading to Boost Hydrogen Co-Production," *Advanced Functional Materials* 31 (2021): 2008812.

38. K. Lakshmanan, W. Huang, S. A. Chala, et al., "Highly Active Oxygen Coordinated Configuration of Fe Single-Atom Catalyst toward Electrochemical Reduction of CO_2 into Multi-Carbon Products," *Advanced Functional Materials* 32 (2022): 2109310.

39. D. Liu, L. Shi, Q. Dai, et al., "Functionalization of Carbon Nanotubes for Multifunctional Applications," *Trends in Chemistry* 6 (2024): 186–210.

40. Y. Xu, R. Xie, Q. Li, et al., "Pyridine Functionalized Carbon Nanotubes: Unveiling the Role of External Pyridinic Nitrogen Sites for Oxygen Reduction Reaction," *Small* 19 (2023): 2302795.

41. H. Singh, M. Marley-Hines, S. Chakravarty, and M. Nath, "Multi-Walled Carbon Nanotube Supported Manganese Selenide as a Highly Active Bifunctional OER and ORR Electrocatalyst," *Journal of Materials Chemistry A* 10 (2022): 6772–6784.

42. Y. Pei, H. Song, Y. Liu, et al., "Boron–Nitrogen-Doped Carbon Dots on Multi-Walled Carbon Nanotubes for Efficient Electrocatalysis of Oxygen Reduction Reactions," *Journal of Colloid and Interface Science* 600 (2021): 865–871.

43. Q. Xue, Y. Wu, J. Hao, et al., "NiO–NiMoO4 Nanocomposites on Multi-Walled Carbon Nanotubes as Efficient Bifunctional Electrocatalysts for Total Water Splitting," *ACS Applied Materials and Interfaces* 15 (2023): 31470–31477.

44. E. Pajootan, S. Omanovic, and S. Coulombe, "Controllable Dry Synthesis of Binder-free Nanostructured Platinum Electrocatalysts Supported on Multi-walled Carbon Nanotubes and Their Performance in the Oxygen Reduction Reaction," *Chemical Engineering Journal* 426 (2021): 131706.

45. M. Tasleem, V. Singh, A. Tiwari, V. Ganesan, and M. Sankar, "Electrocatalysis Using Cobalt Porphyrin Covalently Linked with Multi-Walled Carbon Nanotubes: Hydrazine Sensing and Hydrazine-Assisted Green Hydrogen Synthesis," *Small* 21 (2025): 2401273.

46. T. Y. Ma, S. Dai, M. Jaroniec, and S. Z. Qiao, "Graphitic Carbon Nitride Nanosheet–Carbon Nanotube Three-Dimensional Porous Composites as High-Performance Oxygen Evolution Electrocatalysts," *Angewandte Chemie, International Edition* 53 (2014): 7281–7285.

47. H. Yang, Q. Lin, C. Zhang, et al., "Carbon Dioxide Electroreduction on Single-atom Nickel Decorated Carbon Membranes with Industry Compatible Current Densities," *Nature Communications* 11 (2020): 593.

48. B. Reuillard, J. Warnan, J. J. Leung, D. W. Wakerley, and E. Reisner, "A Poly(Cobaloxime)/Carbon Nanotube Electrode: Freestanding Buckypaper with Polymer-Enhanced H_2-Evolution Performance," *Angewandte Chemie, International Edition* 55 (2016): 3952–3957.

49. Y. Meng, J. Li, S. Zhao, et al., "Fluorination-Assisted Preparation of Self-Supporting Single-Atom Fe-N-Doped Single-Wall Carbon Nanotube Film as a Bifunctional Oxygen Electrode for Rechargeable Zn–Air Batteries," *Applied Catalysis B: Environment* 294 (2021): 120239.

50. Z. Zhao, F. Wang, B. Li, et al., "Rational Fabrication Strategies of Freestanding/Binder-Free Electrodes for Efficient Capacitive Deionization," *Materials Advances* 4 (2023): 2247–2268.

51. Y. Y. How, A. Numan, M. N. Mustafa, R. Walvekar, M. Khalid, and N. M. Mubarak, "A Review on the Binder-Free Electrode Fabrication for Electrochemical Energy Storage Devices," *Journl of Energy Storage* 51 (2022): 104324.

52. G. Di Liberto, L. Giordano, and G. Pacchioni, "Predicting the Stability of Single-Atom Catalysts in Electrochemical Reactions," *ACS Catalysis* 14 (2024): 45–55.

53. N. Cheng, L. Zhang, K. Doyle-Davis, and X. Sun, "Single-Atom Catalysts: from Design to Application," *Electrochemical Energy Reviews* 2 (2019): 539–573.

54. N. Allasia, S. M. Collins, Q. M. Ramasse, and G. Vilé, "Hidden Impurities Generate False Positives in Single Atom Catalyst Imaging," *Angewandte Chemie, International Edition* 63 (2024): 202404883.

55. J. Luo, V. Ruta, I. S. Kwon, et al., "Fabricating a Structured Single-Atom Catalyst via High-Resolution Photopolymerization 3D Printing," *Advanced Functional Materials* 34 (2024): 2404794.

56. W. S. Hummers and R. E. Offeman, "Preparation of Graphitic Oxide," *Journal of American Chemical Society* 80 (1958): 1339–1339.

57. P. Swift, "Adventitious Carbon - the Panacea for Energy Referencing?," *Surface and Interface Analysis* 4 (1982): 47–51.

58. E. Barsoukov and J. R. Macdonald, *Impedance Spectroscopy: Theory, Experiment, and Applications* (Wiley, 2018).

59. Y. Zhang, T. Mori, J. Ye, and M. Antonietti, "Phosphorus-Doped Carbon Nitride Solid: Enhanced Electrical Conductivity and Photocurrent Generation," *Journal of American Chemical Society* 132 (2010): 6294–6295.

60. S. Biswas, A. Pal, and T. Pal, "Supported Metal and Metal Oxide Particles with Proximity Effect for Catalysis," *RSC Advances* 10 (2020): 35449–35472.

61. J. Liu, M. J. Casavant, M. M. Cox, et al., "Controlled Deposition of Individual Single-Walled Carbon Nanotubes on Chemically Functionalized Templates," *Chemical Physics Letters* 303 (1999): 125–129.

62. K. D. Ausman, R. D. Piner, O. Lourie, R. S. Ruoff, and M. Korobov, "Organic Solvent Dispersions of Single-Walled Carbon Nanotubes: toward Solutions of Pristine Nanotubes," *Journal of Physical Chemistry B* 104 (2000): 8911–8915.

63. F. Inam, H. Yan, M. J. Reece, and T. Peijs, "Dimethylformamide: an Effective Dispersant for Making Ceramic–Carbon Nanotube Composites," *Nanotechnology* 19 (2008): 195710–195710.

64. T. A. Gazis, S. Palit, L. A. Cipriano, et al., "Copper Single-Atom Catalyst for Efficient C–S Coupling in Thioether Synthesis," *Angewandte Chemie, International Edition* 64 (2025): 202510632.

65. J. H. Lehman, M. Terrones, E. Mansfield, K. E. Hurst, and V. Meunier, "Evaluating the Characteristics of Multiwall Carbon Nanotubes," *Carbon* 49 (2011): 2581–2602.

66. N. Kouklin, M. Tzolov, D. Straus, A. Yin, and J. M. Xu, "Infrared Absorption Properties of Carbon Nanotubes Synthesized by Chemical Vapor Deposition," *Applied Physics Letters* 85 (2004): 4463–4465.

67. X. He, X. Xu, G. Bo, and Y. Yan, "Studies on the Effects of Different Multiwalled Carbon Nanotube Functionalization Techniques on the Properties of Bio-Based Hybrid Non-Isocyanate Polyurethane," *RSC Advances* 10 (2020): 2180–2190.

68. B. Ravel and M. Newville, "ATHENA, ARTEMIS, HEPHAESTUS: Data Analysis for X-Ray Absorption Spectroscopy Using IFEFFIT," *Journal Synchrotron Radiation* 12 (2005): 537–541.

69. Y. Joly, "X-Ray Absorption near-Edge Structure Calculations beyond the Muffin-Tin Approximation," *Physical Review B* 63 (2001): 125120.

70. J. Liu, Y. Zou, D. Cruz, A. Savateev, M. Antonietti, and G. Vilé, "Ligand–Metal Charge Transfer Induced *via* Adjustment of Textural Properties Controls the Performance of Single-Atom Catalysts during Photocatalytic Degradation," *ACS Applied Materials and Interfaces* 13 (2021): 25858–25867.

71. G. Vilé, G. Di Liberto, S. Tosoni, et al., "Azide-Alkyne Click Chemistry over a Heterogeneous Copper-Based Single-Atom Catalyst," *ACS Catalysis* 12 (2022): 2947–2958.

72. E. Alwin, W. Nowicki, R. Wojcieszak, M. Zieliński, and M. Pietrowski, "Elucidating the Structure of the Graphitic Carbon Nitride Nanomaterials via X-Ray Photoelectron Spectroscopy and X-Ray Powder Diffraction Techniques," *Dalton Transactions* 49 (2020): 12805–12813.

73. N. Allasia, S. Xu, S. F. Jafri, et al., “Resolving the Nanostructure of Carbon Nitride-Supported Single-Atom Catalysts,” *Small* 21 (2025): 2408286.

74. S. Chen, M. Zhang, P. Zou, B. Sun, and S. Tao, “Historical Development and Novel Concepts on Electrolytes for Aqueous Rechargeable Batteries,” *Energy and Environmental Science* 15 (2022): 1805–1839.

75. A. Van der Ven, K. A. See, and L. Pilon, “Hysteresis in Electrochemical Systems,” *Battery Energy* 1 (2022): 20210017.

76. P. Alfonso-Súarez, A. V. Kolliopoulos, J. P. Smith, C. E. Banks, and A. M. Jones, “An Experimentalist’s Guide to Electrosynthesis: the Shono Oxidation,” *Tetrahedron Letters* 56 (2015): 6863–6867.

77. R. G. Compton and C. E. Banks, *Understanding Voltammetry*, 2nd ed. (Imperial College Press, 2011).

78. G. Chen, C. C. Waraksa, H. Cho, D. D. Macdonald, and T. E. Mallouka, “EIS Studies of Porous Oxygen Electrodes with Discrete Particles,” *Journal of Electrochemical Society* 150 (2003): E423.

79. M. de Pauli, A. M. C. Gomes, R. L. Cavalcante, et al., “Capacitance Spectra Extracted from EIS by a Model-Free Generalized Phase Element Analysis,” *Electrochimica Acta* 320 (2019): 134366.

80. E. P. Randviir and C. E. A. Banks, “Review of Electrochemical Impedance Spectroscopy for Bioanalytical Sensors,” *Analytical Methods* 14 (2022): 4602–4624.

Supporting Information

Additional supporting information can be found online in the Supporting Information section.

Supporting File: admi70363-sup-0001-SuppMat.pdf